Check for updates

MACl enhanced electron extraction in all-inorganic Cs$_2$AgBiBr$_6$ perovskite photovoltaics†

Jinxia Duan,[ab] Yi Yang, [ID][a] Jie Tang,[a] Houzhao Wan, [ID][ab] Guokun Ma,[ab] Liangping Shen,[ab] Jun Zhang,[ab] Hao Wang [ID] ★[ab] and Hai Zhou [ID] ★[ac]

We present organic-halide treatment in advance to maximize electron extraction of Cs$_2$AgBiBr$_6$ double perovskite solar cells. Through optimizing the organic halide and concentration systematically, the best carbon-based Cs$_2$AgBiBr$_6$ perovskite solar cell fabricated in an airing chamber achieves a power conversion efficiency of 2.03% and shows excellent long-term stability in air over 30 days.

Halide perovskite materials have become one of the most competitive photovoltaic materials owing to their exceptional photoelectrical characteristics, such as large absorption coefficient, adjustable bandgap, high carrier mobility and long carrier diffusion length. Representative organic–inorganic hybrid perovskite solar cells (PeSCs) show outstanding photoelectric conversion ability. To date, the power conversion efficiency (PCE) has leapt to 25.8% (certified 25.5%).[1,2] Unfortunately hybrid PeSCs contain lead and organic ions, resulting in poor device stability and environmental toxicity, which seriously hinder large-scale production and commercialization of PeSCs. Inorganic cations replacing organic cations and two heterovalent cations taking over divalent lead ions have been proposed to enhance the inherent stability and decrease heavy metal toxicity.[3–6] The concept of a fully inorganic lead-free double perovskite with the formula of A$_2$B$^+$B$'^{3+}$X$_6$ conforms to this situation. According to the first principle calculation, Cs$_2$AgBiBr$_6$ is a double perovskite alternative to toxic and unstable hybrid PeSCs because of its high stability and long carrier lifetime.[6–8]

Slavney *et al.*[9] presented that Cs$_2$AgBiBr$_6$ had terrible potential optical and physical properties, which motivated further exploration of double perovskites for photovoltaic applications. Greul *et al.* prepared Cs$_2$AgBiBr$_6$ films by a spin-coating

method and incorporated them into photovoltaic devices in 2017.[10] The Cs$_2$AgBiBr$_6$-based PeSC showed PCE of 2.43% and open circuit voltage (V_{oc}) exceeding 1 V, which was the highest V_{oc} for perovskite containing bismuth at that time. This work pointed out a promising class of perovskites for the photovoltaic field. However, the efficiency of Cs$_2$AgBiBr$_6$ PeSCs was limited by their wide indirect bandgap and high inherent defects. Increasing the light capture and crystalline quality of Cs$_2$AgBiBr$_6$ film is a considerable challenge to further improve Cs$_2$AgBiBr$_6$ device performances.[10–13] Photosensitizers (such as dyes and organic materials) have been introduced to broaden the absorption spectrum and raise the device PCE of Cs$_2$AgBiBr$_6$ perovskite.[11–13] For example, Yang *et al.*[11] used an N719 interlayer to broaden the absorption and heighten the PCE to 2.84%. Wang *et al.*[12] improved the light absorption of Cs$_2$AgBiBr$_6$ films by D149 dye treatment of the electron transport layer (ETL). Nevertheless, dye intermediates failed to improve the poor crystallinity of Cs$_2$AgBiBr$_6$ itself, and affect the internal resistance of the device, resulting in the decrease of the fill factor (FF).

In addition, expensive organic hole transport materials (HTMs) are very vulnerable to the migration of halide ions.[14] The carbon electrode materials replacing the HTM and metal electrode are relatively mature in related fields. Cs$_2$AgBiBr$_6$ PeSCs based on carbon electrodes have seen some attempts.[15,16] For example, Li *et al.* fabricated a Cs$_2$AgBiBr$_6$ PeSC with the efficiency of 2.57% and excellent high-temperature and air stability.[15] Li *et al.*[16] employed ionic liquids (ILs) to inhibit Br$^-$ migration effectively, thereby reducing film defects and improving energy level matching. A carbon-based Cs$_2$AgBiBr$_6$ PeSC achieved a PCE of 2.22% and positive long-term stability. These provide convenient and efficient strategies to raise the efficiency and stability of environmentally friendly Cs$_2$AgBiBr$_6$-based photovoltaics.

Undesirable performances of Cs$_2$AgBiBr$_6$ photovoltaics are due to their deep electron defects.[15,17] The passivation for the ETL/perovskite interface by methylammonium chloride is an aid to improve the crystallization of Cs$_2$AgBiBr$_6$ film and electron extraction capability.[18,19] In this work, we introduce methylammonium halide (MAX) to ameliorate the ETL/perovskite

[a] School of Microelectronics, Hubei University, Wuhan 430062, P. R. China. E-mail: wangh@hubu.edu.cn
[b] Hubei Yangtze Memory Laboratories, Wuhan 430205, P. R. China
[c] International School of Microelectronics, Dongguan University of Technology, Dongguan, Guangdong, 523808, P. R. China. E-mail: hizhou@dgut.edu.cn

interface and perovskite quality. Three MAXs are employed to explore systematically the role of charge transport and perovskite crystallization.

The concentration of the $Cs_2AgBiBr_6$ precursor solution is 0.5 M. After finishing the growth of TiO_2 NRs, 0.25 M-MAX solution was spin-coated in advance on the TiO_2 ETL followed by spin-coating the $Cs_2AgBiBr_6$ precursor. The entire preparation procedure of $Cs_2AgBiBr_6$ film was carried out in an airing chamber and drawn with a diagram in Fig. S1 (ESI†). Cs_2Ag-$BiBr_6$ films with uniform yellow appearance (optical image illustration is in Fig. S1, ESI†) were obtained after 280 °C annealing. $Cs_2AgBiBr_6$ film without pre-treatment was prepared as a reference sample. In order to verify the effect of MAX pre-treatment on the morphologies of $Cs_2AgBiBr_6$ films, the surface of the samples was observed by a Scanning Electron Microscope (SEM). SEM images of $Cs_2AgBiBr_6$ films with MAX pre-treatment (including the reference, MACl, MABr and MAI pre-treatment) were exhibited in Fig. 1 using low magnification and high magnification. $Cs_2AgBiBr_6$ samples with MACl, MABr and MAI pre-treatment were named $Cs_2AgBiBr_6$-MACl, $Cs_2AgBiBr_6$-MABr and $Cs_2AgBiBr_6$-MAI, respectively. From SEM images, rather more regular grains were observed in $Cs_2AgBiBr_6$ films with MAX pre-treatment than reference $Cs_2AgBiBr_6$. Among four $Cs_2AgBiBr_6$ films, $Cs_2AgBiBr_6$-MACl has the smoothest surface and the most uniform grains. The pin-holes and/or cracks were marked by circles in other $Cs_2AgBiBr_6$ films.

In the X-ray diffraction (XRD) spectra of Fig. S2a (ESI†), all samples presented $Cs_2AgBiBr_6$ characteristic peaks.[13,15] The full-width half-maximum (FWHM) of the reference, Cs_2Ag-$BiBr_6$-MACl, $Cs_2AgBiBr_6$-MABr and $Cs_2AgBiBr_6$-MAI was 0.131°, 0.124°, 0.128° and 0.126° based on the (220) plane at $\sim$22.12°. The narrow FWHM of $Cs_2AgBiBr_6$-MACl suggested its largest grain size among the four $Cs_2AgBiBr_6$ samples,[12] which was in accordance with the SEM observation in Fig. 1. Fig. S2b (ESI†) displays the ultraviolet-visible (UV-vis) absorption spectra of the $Cs_2AgBiBr_6$ samples. The absorption peak was at $\sim$439 nm for the $Cs_2AgBiBr_6$ samples. The absorption intensity followed the order: $Cs_2AgBiBr_6$-MACl > $Cs_2AgBiBr_6$-MAI > $Cs_2AgBiBr_6$-MABr > the reference. $Cs_2AgBiBr_6$-MACl had the highest absorption intensity and the broadest absorption edge. The bandgap energy calculation is shown in the Tauc diagram of Fig. S2b (ESI†). $Cs_2AgBiBr_6$-MACl had narrow direct and indirect bandgaps. Steady-state photoluminescence (PL) spectra in Fig. S2c (ESI†) showed that all $Cs_2AgBiBr_6$ samples had an emission peak at $\sim$520 nm, according to the direct bandgap. TiO_2/$Cs_2AgBiBr_6$-MACl film had the lowest emission, which suggested its high crystalline quality and low defect density.[15,20] Fig. S2d (ESI†) exhibits the time resolved photoluminescence (TRPL) spectra of TiO_2/$Cs_2AgBiBr_6$ films. The carrier recombination lifetime (τ) fitting data are displayed in Table S1 (ESI†). The lifetime of the reference, $Cs_2AgBiBr_6$-MACl, $Cs_2AgBiBr_6$-MABr and $Cs_2AgBiBr_6$-MAI samples was 59.46 ns, 42.53 ns, 48.53 ns and 45.0 ns, respectively. The smallest lifetime of $Cs_2AgBiBr_6$-MACl indicated its fast electron transfer and low trap recombination.[21] To elucidate the chemical state of $Cs_2AgBiBr_6$ films, the X-ray photoelectron spectroscopy (XPS) spectra are shown in Fig. S3 and S4 (ESI†). The expected elements were found in scanning XPS measurement of the $Cs_2AgBiBr_6$ films.[20] The orbital binding energy of element Ag, Bi and Br for $Cs_2AgBiBr_6$-MACl shifted slightly towards the high binding energy direction, while the binding energy of Cs3d did not shift. The chemical bonding interaction of Cs-Br, Br-Bi and Br-Ag was enhanced for $Cs_2AgBiBr_6$-MACl, verified by Fourier transform infrared (FT-IR) measurement. This was beneficial to improving the stability of $Cs_2AgBiBr_6$ PeSCs.

HTM-free PeSCs using carbon as the top electrode were fabricated with the structure of FTO/TiO_2/$Cs_2AgBiBr_6$/carbon. A typical diagrammatic sketch and cross-sectional image of the $Cs_2AgBiBr_6$-MACl device are shown in Fig. 2a. The J–V curves of the $Cs_2AgBiBr_6$ devices are depicted in Fig. 2b. The $Cs_2AgBiBr_6$-MACl PeSC had a significantly improved short-circuit current density (J_{sc}) of 3.04 mA cm^{-2} and FF of 62% compared to reference PeSC, resulting in the efficiency reaching 2.03%. The efficiency of the $Cs_2AgBiBr_6$ devices was in the order of Cs_2Ag-$BiBr_6$-MACl > $Cs_2AgBiBr_6$-MAI > $Cs_2AgBiBr_6$-MABr > the reference. The PCE of the $Cs_2AgBiBr_6$-MACl device is the highest, which is 68% higher than that of the reference PeSC. The best and average photovoltaic parameters of the $Cs_2AgBiBr_6$ devices are summarized in Table S2 (ESI†). As shown in Fig. 2c, the reverse and forward scanning (RE and FW) J–V curves were diagrammed for the champion devices. The hysteresis index (HI) was further quantified according to the formula[21]
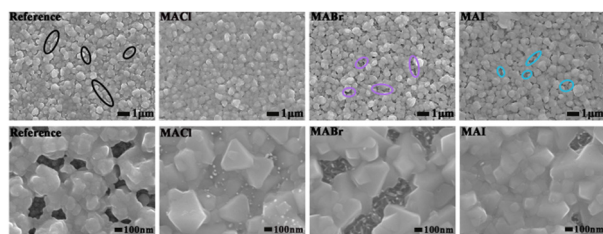

Fig. 1 SEM images of the reference and the samples pre-treated with MAX.
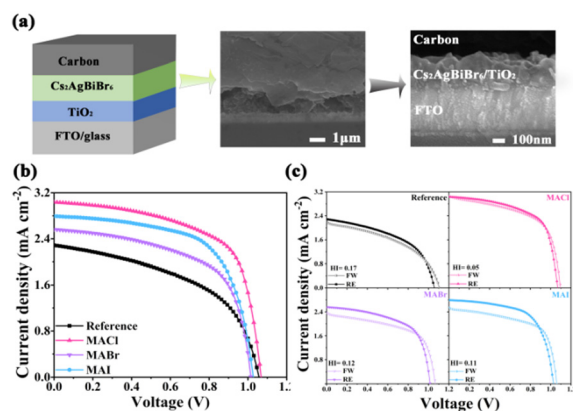

Fig. 2 (a) Scheme and SEM sectional images of the device structure. (b) J–V curves of the champion devices. (c) RE and FW J–V curves for the best devices.
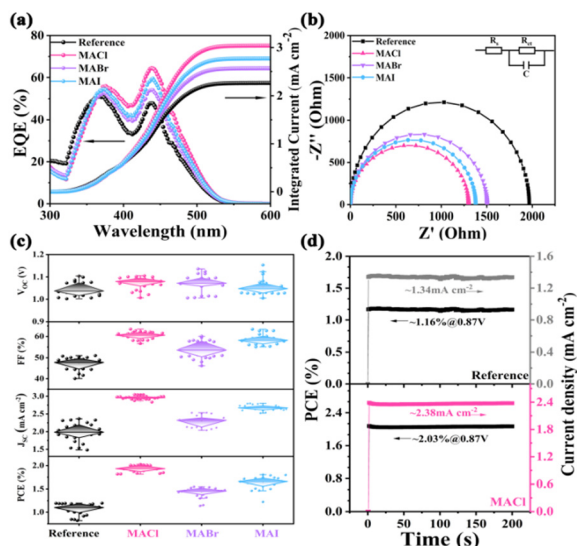
Fig. 3 (a) The EQE and integrated current density curves of the PSCs. (b) Nyquist EIS spectra (the inset is the equivalent circuit). (c) Box charts of V_{oc}, FF, J_{sc} and PCE. (d) Steady-state power outputs at the maximum power point of the reference and $Cs_2AgBiBr_6$-MACl.

$$HI = [J_{RE}(0.8\ V_{oc}) - J_{FW}(0.8\ V_{oc})]/J_{FW}(0.8\ V_{oc}) \qquad (1)$$

where $J_{RE}(0.8\ V_{oc})$ and $J_{FW}(0.8\ V_{oc})$ are the current-densities at $0.8\ V_{oc}$ in reverse and forward scanning, respectively. The HI of the $Cs_2AgBiBr_6$-MACl device decreased to 0.05 from 0.17 for the reference PeSC.

Fig. 3a portrays the external quantum efficiency (EQE) spectra of the $Cs_2AgBiBr_6$ PeSCs. In the wavelength range of 350–550 nm, the $Cs_2AgBiBr_6$-MACl PeSC had the highest EQE value among the four $Cs_2AgBiBr_6$ cells. The EQE of the $Cs_2AgBiBr_6$-MACl PeSC was 65% at 440 nm, which was 15% more than that of the reference PeSC. The calculated integral current density was from 2.27 mA cm^{-2} in the reference PeSC to 3.01 mA cm^{-2} in the $Cs_2AgBiBr_6$-MACl device, which corresponded to the J–V results in Fig. 2b. The $Cs_2AgBiBr_6$-MACl device obtained the highest current density. To further explore the raised FF and J_{sc} related to charge transport at the interface and interior of the PeSCs, electrochemical impedance spectroscopy (EIS) tests were carried out. Nyquist spectra of four PeSCs were plotted in Fig. 3b and the corresponding equivalent circuit was illustrated. The fitted data are summarized in Table S3 (ESI†), where R_s represents the series resistance of the devices, R_{ct} is the interfacial charge transport resistance and C refers to the capacitance. R_{ct} was arranged in the following order: the reference > $Cs_2AgBiBr_6$-MABr > $Cs_2AgBiBr_6$-MAI > $Cs_2AgBiBr_6$-MACl. The R_{ct} values were calculated to be 1.99 kΩ, 1.51 kΩ, 1.36 kΩ and 1.27 kΩ, respectively. Significantly reduced R_{ct} indicates superior charge collection, rendering improved FF and diminished HI in the $Cs_2AgBiBr_6$-MACl and $Cs_2AgBiBr_6$-MAI devices.[12,16] Hence, $Cs_2AgBiBr_6$-MACl had the champion efficiency combined with the highest J_{sc}. The statistical photovoltaic parameters of the $Cs_2AgBiBr_6$ devices were summarized in Table S2 (ESI†) and Fig. 3c. The increase of J_{sc} and FF produced high PCE in the $Cs_2AgBiBr_6$-MACl devices. To verify

whether the PeSCs stabilize the output power under the irradiation of AM1.5G standard sunlight, the steady-state photocurrent and efficiency at the maximum power point (MPP) were further characterized in the air environment, as shown in Fig. 3d. The voltage at the maximum power point (V_{mpp}) of the $Cs_2AgBiBr_6$-MACl device was 0.87 V, and the steady J_{sc} and PCE are 2.38 mA cm^{-2} and 2.03%, which were much higher than those of the reference device (1.34 mA cm^{-2} and 1.16%). The photoelectric conversion curves of the MAX pre-treated devices under continuous light within 200s were smoother than that of the reference device, indicating better interface contact of ETL/perovskite in the PeSCs with MAX pre-treatment. The trap density (N_{trap}) was calculated by the space charge limited current (SCLC) model to be 1.468×10^{15} m^{-3}, 9.737×10^{14} m^{-3}, 1.312×10^{15} m^{-3} and 1.27×10^{15} m^{-3} for the reference, $Cs_2AgBiBr_6$-MACl, $Cs_2AgBiBr_6$-MABr and $Cs_2AgBiBr_6$-MAI, respectively. The dark J–V curves were measured and plotted in Fig. S8 (ESI†) to unravel the working mechanism of the devices. The $Cs_2AgBiBr_6$-MACl PeSC had the lowest saturation current and relatively large shunt resistance (R_{sh}) among the four $Cs_2AgBiBr_6$ devices, which suggested that the $Cs_2AgBiBr_6$-MACl PeSC had high electron extraction and low defect recombination. This was in line with the absorption, PL, EIS, defect and J–V results.

Based on these results, the mechanism of $Cs_2AgBiBr_6$-MACl was speculated. At the initial stage, MA^+ and Cl^- ions participated in the double perovskite crystallization, producing the formation of $Cs_{2-x}MA_xAgBiBr_{6-y}Cl_y$ ($0 < x < 1.0$, $0 < y < 1.0$) intermediate phase. With the volatilization of MA^+ and Cl^- ions during heat treatment, the $Cs_{2-x}MA_xAgBiBr_{6-y}Cl_y$ intermediate phase transformed to the ultimate $Cs_2AgBiBr_6$. Adequate volatile additive can promote crystal growth, which resulted in superior film morphology by altering the activation energy of the perovskite crystallization.[22,23] Consequently, MACl delayed the crystallization progression of $Cs_2AgBiBr_6$ perovskites, resulting in large grain sizes and low trap density for $Cs_2AgBiBr_6$-MACl.
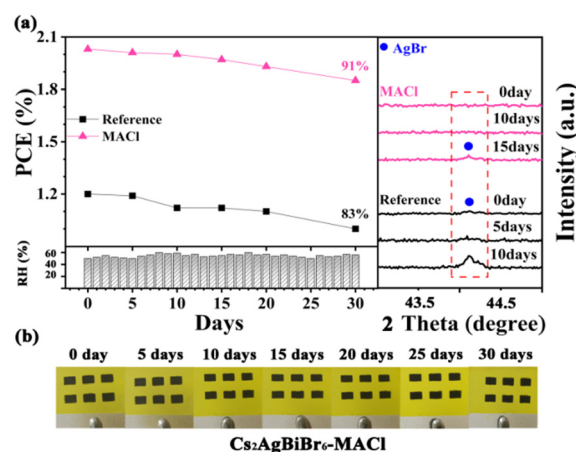

Fig. 4 (a) Statistical diagram of the efficiency change for the devices stored in the environment with a temperature of 28 °C and a relative humidity of 50–60% during 30 days. The right is the change of the XRD patterns of the devices. (b) Appearance change diagram of the $Cs_2AgBiBr_6$-MACl device within 30 days.

Table 1 Recent progress of carbon-based $Cs_2AgBiBr_6$ PeSCs

Device structure	PCE	Fabrication	Long-term stability	Ref.
$FTO/m\text{-}TiO_2/Cs_{1.99}Li_{0.01}Cs_2AgBiBr_6/C$	2.57%	N2 glove box	80%, 25 °C, 5%RH, 90 days 80%, 85 °C, 0%RH, 60 days	15
$FTO/TiO_2NRs/Cs_2(Ag_{1-x}Zn_x)BiBr_6/C$	2.16%	N2 glove box	90%, 25 °C, 40%RH, 14 days in ambient air	21
$FTO/TiO_2NRs/BMPyrCl/Cs_2AgBiBr_6/C$	2.22%	N2 glove box	~100%, 25 °C, 40% ± 5%RH, 40 days in ambient air.	16
$FTO/m\text{-}TiO_2/Cs_2AgBiBr_6/SnS\ QDs/C$	1.95%	N2 glove box	90%, 42 h in ambient air.	23
$FTO/TiO_2NRs/Cs_2AgBiBr_6\text{-}MACl/C$	2.03%	Airing chamber	90%, 28 °C, 50%–60%RH, 30 days in ambient air	This work

Moreover, the strong MA^+/TiO_2 interaction compared to inorganic ion/TiO_2 brought higher quality double perovskite film and faster electron extraction in the perovskite PeSC.[19] Impurity phase containing chlorine caused by excess MAX would hinder charge transport, which was confirmed by the inferior performance of $Cs_2AgBiBr_6$-0.5MACl (shown in Fig. S9, ESI†).

In order to investigate the effect of MACl pre-treatment on the performance stability of the PeSCs, the unpackaged reference and $Cs_2AgBiBr_6$-MACl samples were monitored by storing them under the air condition of 28 °C and relative humidity of 50–60% for 30 days. The PCE and XRD results are shown in Fig. 4a and Table S5 (ESI†). By tracking the PCE changes of the PeSCs, the $Cs_2AgBiBr_6$-MACl device maintained more than 90% of the initial PCE, while the reference device maintained 83% of the initial efficiency. AgBr miscellaneous phase was detected for the reference on the fifth day and aggravated on the tenth day by XRD monitoring in Fig. 4a, which was considered as an evil to deteriorate device performance. AgBr impure phase appeared after 15 days for the $Cs_2AgBiBr_6$-MACl device. No significant change of the $Cs_2AgBiBr_6$-MACl film was monitored in the appearance during preservation, which was displayed in photos of the samples during storing for 30 days. The $Cs_2AgBiBr_6$-MACl sample had better stability because of its higher perovskite crystalline degree than the reference sample. In addition, the hydrophobicity of the carbon electrode provides protection for the perovskite films, which further improves the environmental stability of the $Cs_2AgBiBr_6$ PeSCs. The entire preparation process being completed in air widened the application fields of $Cs_2AgBiBr_6$ perovskite (Table 1).

In summary, we fabricated efficient and stable $Cs_2AgBiBr_6$ PeSCs by introducing MAX pre-treatment to modify the ETL/$Cs_2AgBiBr_6$ interface and perovskite crystalline quality. The $Cs_2AgBiBr_6$ with three MAX pre-treatment was studied in an airing chamber systematically. The MACl modifier can bond with the ETL and perovskite and enhance perovskite crystallization. MACl modification facilitated electron extraction from the perovskite to the ETL, which reduced the trap-assisted recombination. As a result, the optimized PeSC with $Cs_2AgBiBr_6$-MACl achieved a PCE of 2.03% with slightly higher J_{sc} and FF than the reference device. Importantly, $Cs_2AgBiBr_6$-MACl exhibited better durability of the resultant PeSCs.

Conflicts of interest

There are no conflicts to declare.

Notes and references

1 M. Kim, J. Jeong, H. Lu, T. K. Lee, F. T. Eickemeyer, Y. Liu, I. W. Choi and S. J. Choi, et al., Science, 2022, 375, 302–306.
2 L. Zhang, X. Pan, L. Liu and L. Ding, J. Semicond., 2022, 43, 030203.
3 B. Wu, W. Ning, Q. Xu, M. Manjappa, M. Feng, S. Ye, J. Fu and S. Lie, et al., Sci. Adv., 2021, 7, eabd3160.
4 Z. Fang, S. Wang, S. Yang and L. Ding, Inorg. Chem. Front., 2018, 5, 1690–1693.
5 W. Hu, X. He, Z. Fang, W. Lian, Y. Shang, X. Li, W. Zhou and M. Zhang, et al., Nano Energy, 2020, 68, 104362.
6 M. T. Sirtl, R. Hooijer, M. Armer, F. G. Ebadi, M. Mohammadi, C. Maheu, A. Weis, B. T. van Gorkom, S. Häringer, R. A. J. Janssen, T. Mayer, V. Dyakonov, W. Tress and T. Bein, Adv. Energy Mater., 2022, 12, 2103215.
7 W. Tress and M. T. Sirtl, Sol. RRL, 2021, 6, 2100770.
8 X. Cai, Y. Zhang, Z. Shi, Y. Chen, Y. Xia, A. Yu, Y. Xu, F. Xie, H. Shao, H. Zhu, D. Fu, Y. Zhan and H. Zhang, Adv. Sci., 2022, 9, e2103648.
9 A. H. Slavney, T. Hu, A. M. Lindenberg and H. I. Karunadasa, J. Am. Chem. Soc., 2016, 138, 2138–2141.
10 E. Greul, Michiel L. Petrus, A. Binek, P. Docampo and T. Bein, J. Mater. Chem. A, 2017, 5, 19972–19981.
11 X. Yang, Y. Chen, P. Liu, H. Xiang, W. Wang, R. Ran, W. Zhou and Z. Shao, Adv. Funct. Mater., 2020, 30, 2001557.
12 L. Yang, P. Hou, B. Wang, C. Dall'Agnese, Y. Dall'Agnese, G. Chen, Y. Gogotsi, X. Meng and X.-F. Wang, Chem. Eng. J., 2022, 446, 136963.
13 B. Wang, N. Li, L. Yang, C. Dall'Agnese, A. K. Jena, S. I. Sasaki, T. Miyasaka, H. Tamiaki and X. F. Wang, J. Am. Chem. Soc., 2021, 143, 2207–2211.
14 Q. Dou, T. Whatley, T. Syed, W. Wei and H. Wang, J. Mater. Chem. A, 2022, 10, 19211–19230.
15 J. Li, J. Duan, J. Du, X. Yang, Y. Wang, P. Yang, Y. Duan and Q. Tang, ACS Appl. Mater. Interfaces, 2020, 12, 47408–47415.
16 J. Li, X. Meng, Z. Wu, Y. Duan, R. Guo, W. Xiao, Y. Zhang, Y. Li, Y. Shen, W. Zhang and G. Shao, Adv. Funct. Mater., 2022, 32, 2112991.
17 F. Ji, Y. Huang, F. Wang, L. Kobera, F. Xie, J. Klarbring, S. Abbrent, J. Brus, C. Yin, S. I. Simak, I. A. Abrikosov, I. A. Buyanova, W. M. Chen and F. Gao, Adv. Funct. Mater., 2020, 30, 2005521.
18 F. Ye, J. Ma, C. Chen, H. Wang, Y. Xu, S. Zhang, T. Wang, C. Tao and G. Fang, Adv. Mater., 2021, 33, e2007126.
19 H. Wu, Y. Wang, A. Liu, J. Wang, B. J. Kim, Y. Liu, Y. Fang, X. Zhang, G. Boschloo and E. M. J. Johansson, Adv. Funct. Mater., 2021, 32, 2109402.
20 P. Hou, W. Yang, N. Wan, Z. Fang, J. Zheng, M. Shang, D. Fu, Z. Yang and W. Yang, J. Mater. Chem. C, 2021, 9, 9659–9669.
21 J. Duan, Q. Yue, Q. Xiong, L. Wang, L. Zhu, K. Zhang, J. Zhang and H. Wang, Appl. Surf. Sci., 2019, 470, 613–621.
22 Y. Ou, Z. Lu, J. Lu, X. Zhong, P. Chen, L. Zhou and T. Chen, Opt. Mater., 2022, 129, 112452.
23 Y. Ou, J. Lu, X. Zhong, X. Li, S. Wu, P. Chen and L. Zhou, Mater. Lett., 2022, 312, 131672.